Dynamic rupture simulation of non-planar faults with a finite-difference approach

V. M. Cruz-Atienza* and J. Virieux

Géosciences Azur, CNRS-UNSA-UPMC-IRD, Sophia Antipolis, France. E-mail: cruz@geoazur.unice.fr

SUMMARY

Two-dimensional (2-D) modelling of dynamic seismic rupture is performed using a recent staggered-grid finite-difference formulation. Rupture boundary conditions are applied only inside the crack, without assuming any symmetry with respect to the rupture surface. By a simple rotation of the stress tensor, the local orientation of the crack is taken into consideration at each stress point. The grid size is controlled by the source discretization. The greater the number of grid nodes discretizing the finite source, the lower the grid size could be. Below the lower bound value associated with a given discretization, numerical artefacts are not negligible with respect to the spatial frequency content of the dynamic solution. Solutions converge for both point and finite sources by densifying the number of stress points in the source. Numerical scaling of boundary conditions is an important element of this convergence and allows the removal of high-frequency spurious effects of dynamic rupture conditions. For the self-similar crack, a comparison with Kostrov's analytical solution shows that accurate stress singularities are obtained for various crack orientations with respect to the numerical grid. For spontaneous rupture modelling assuming a slip-weakening constitutive law, similar solutions are found for both rupture kinematics and excited wavefield in planar faults with any orientation. Finally, based on these results, rupture propagation over an arbitrary non-planar fault is justified and then performed in the presence of heterogeneous medium.

Key words: boundary conditions, dynamic rupture, finite-difference modelling, non-planar faults, seismic rupture, seismic source modelling.

GJI Seismology

1 INTRODUCTION

Dynamic modelling of seismic rupture has been performed applying different numerical tools such as finite-difference (FD) methods (Madariaga 1976), finite-element (FE) methods (Day 1977) and boundary integral equation (BIE) methods (Das & Aki 1977; Andrews 1985). The last approach seems the most appropriate for solving the boundary problem of seismic source dynamics because integral equations discretize only boundary structures. The stress field must be specified on a given discretized surface at time *t*. Nevertheless, the analytical construction of Green's functions is required representing an important limitation of these methods: it is not possible to embed the dynamic source in a heterogeneous medium. In spite of this limitation, the BIE methodology has been successfully used to simulate non-planar seismic sources, showing how important it is for rupture history to consider realistic source geometries (Aochi & Fukuyama 2002). Moreover, application of FE methods has shown that rupture dynamics is largely influenced in dipping faults by the interaction with the free surface and by the two-way interaction between non-parallel fault segments (Oglesby *et al.* 2000,

2003). Thus, complex source geometry seems to be determinant in rupture evolution. On the other hand, simulations with FD approaches have revealed that heterogeneous surrounding media can also strongly affect the source dynamics. For instance, the presence of low-velocity zones acts directly on both rupture front velocity and fault slip (Mikumo *et al.* 1987; Harris & Day 1997). If rupture governed by Coulomb friction propagates within a compliant fault zone, the strength and shape of the slip pulse will strongly depend on the elastic properties and geometry of such a zone (Ben-Zion & Huang 2002). Furthermore, observational evidence of ground motion in some remarkable cases can only be explained if realistic heterogeneous structures are taken into account during simulations (e.g. Olsen 2000; Shapiro *et al.* 2000). However, until now only planar source boundary conditions have been applied in FD methods to keep numerical errors under control. This constraint has precluded such approaches from considering different fault geometries. Is it possible to implement intricate source geometries in a FD approach? If so, we contribute toward finding more realistic simulations by considering arbitrary heterogeneous media, composite friction laws and complex source geometries.

We present a new approach to the modelling of dynamic faulting with any pre-established source geometry based in a FD

*Consejo Nacional de Ciencia y Tecnología (CONACyT), México.

formulation. We consider a new spatial stencil proposed by Saenger *et al.* (2000). Stress boundary conditions with numerical scaling features represent the source inside the numerical grid. This is our original contribution. Accurate estimations of elastic fields are observed near the crack tip. We first introduce the elastodynamic equations for in-plane cracks in two dimensions, as well as the FD technique we use. Afterwards, boundary conditions are discussed in a separate section. We show how rupture simulations of planar sources allow us to validate and estimate the accuracy of seismic source and wave modelling. Finally, we discuss the case of a simple scenario that includes a non-planar source traversing a single heterogeneity in the elastic medium, mainly to illustrate our new approach.

2 ELASTODYNAMIC EQUATIONS FOR AN ARBITRARY CRACK

Let us consider the following two-dimensional (2-D) velocity–stress formulation of elastodynamic equations:

$$\rho\frac{\partial v_x}{\partial t} = \frac{\partial \tau_{xx}}{\partial x} + \frac{\partial \tau_{xz}}{\partial z}$$

$$\rho\frac{\partial v_z}{\partial t} = \frac{\partial \tau_{xz}}{\partial x} + \frac{\partial \tau_{zz}}{\partial z}$$

$$\frac{\partial \tau_{xx}}{\partial t} = (\lambda + 2\mu)\frac{\partial v_x}{\partial x} + \lambda\frac{\partial v_z}{\partial z}$$

$$\frac{\partial \tau_{zz}}{\partial t} = \lambda\frac{\partial v_x}{\partial x} + (\lambda + 2\mu)\frac{\partial v_z}{\partial z}$$

$$\frac{\partial \tau_{xz}}{\partial t} = \mu\left(\frac{\partial v_z}{\partial x} + \frac{\partial v_x}{\partial z}\right) \tag{1}$$

for modelling *P-SV* wave propagation (Virieux 1986). We assume a 2-D medium with Cartesian coordinate axes x and z pointing to the right and down respectively. The medium is linearly elastic and isotropic: it is fully described by λ and μ, the Lamé coefficients, and ρ, the density. The particle velocity vector is denoted by (v_x, v_z), while the second-order stress tensor is denoted by $(\tau_{xx}, \tau_{zz}, \tau_{xz})$. The velocity–stress system (1) can be discretized by using a staggered grid in order to calculate spatial derivatives half-way between two gridpoints. Madariaga (1976) has proposed an elementary structure for such a grid (Fig. 1a) that has become a standard procedure in elastic wave propagation. The stencil structure is uniquely determined by the definition of the spatial differential operators. Authors have developed various schemes following the same staggered-grid strategy in order to improve the accuracy of numerical simulations in elastic wave propagation (see Virieux 1986; Levander 1988, among others). Furthermore, many people have successfully used this numerical approach for modelling dynamic propagation of planar cracks (e.g. Virieux & Madariaga 1982; Olsen *et al.* 1997; Madariaga *et al.* 1998; Peyrat *et al.* 2001). However, the stencil associated with this formulation has one major disadvantage: neither normal and tangential stresses nor the two velocity components are defined in the same grid node (Fig. 1a). This limitation has prevented authors from applying boundary conditions to an arbitrary oriented crack. In order to avoid this problem, the stencil should be conceived in a different way. We define the partial differential operators D_x, along coordinate x, and D_z, along coordinate z, as follows:

$$D_x(f_{ij}) = \frac{1}{2h}\left(f_{i+\frac{1}{2},j+\frac{1}{2}} - f_{i-\frac{1}{2},j-\frac{1}{2}} + f_{i+\frac{1}{2},j-\frac{1}{2}} - f_{i-\frac{1}{2},j+\frac{1}{2}}\right)$$

$$D_z(f_{ij}) = \frac{1}{2h}\left(f_{i+\frac{1}{2},j+\frac{1}{2}} - f_{i-\frac{1}{2},j-\frac{1}{2}} - f_{i+\frac{1}{2},j-\frac{1}{2}} + f_{i-\frac{1}{2},j+\frac{1}{2}}\right) \tag{2}$$
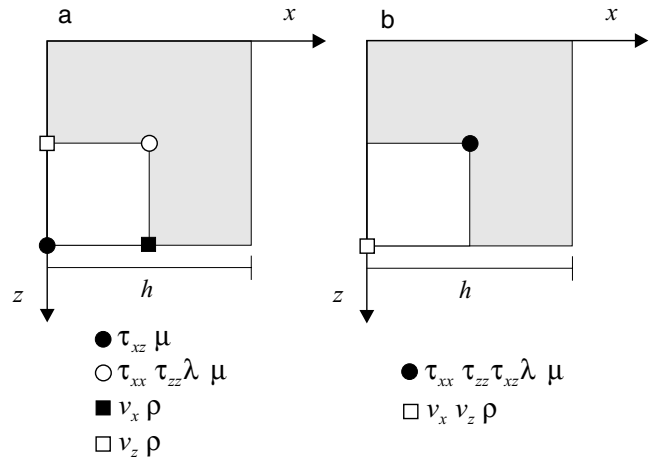
Figure 1. Staggered-grid numerical stencils for (a) the standard finite-difference approach (Madariaga 1976), and for (b) the new finite-difference approach (Saenger *et al.* 2000) used in this work. h is the grid size, $(\tau_{xx}, \tau_{zz}, \tau_{xz})$ is the second-order stress tensor, (v_x, v_z) is the particle velocity vector, λ and μ are the Lamé coefficients, and ρ is the density.

which correspond to the same stencil as the one introduced by Saenger *et al.* (2000) (see Appendix A). The associated staggered grid is unique (Fig. 1b) and defines the stress components at a single grid node. Similarly, velocity components are defined at a single node shifted half-way in both x and z directions. In the present work we have applied operators accurate to fourth-order in space increments (Appendix A) and to second-order in time increments as the best compromise between accuracy of wavefields and memory requirement to solve the system (1). We emphasize that this new finite-difference approach retains the accuracy of the staggered grid: one must estimate stress derivatives at velocity gridpoints and, conversely, velocity derivatives at stress locations. On the whole, the three main advantages of the new approach with respect to the standard one are: the reduction of numerical-grid dispersion along preferred directions, a less restrictive numerical stability criterion (Saenger *et al.* 2000), and definition of the stress and velocity fields separately in only two staggered grids. Thanks to this particular wavefield discretization, we are able to apply boundary conditions for any crack orientation in specific nodes. The way we impose such boundary conditions will be described in the next section. In order to simulate an unbounded space, we have implemented the standard perfectly matched layer (PML) absorbing boundary conditions in the external edges of the computational domain (Berenger 1994; Hastings *et al.* 1996).

3 CRACK BOUNDARY CONDITIONS

Considering planar crack geometries may reduce the computational effort by a factor of 2 when the problem is symmetric. This is the case when modelling a half-space bounded by the plane containing the crack (e.g. Madariaga 1976; Das & Aki 1977). This fact has led authors to introduce Cauchy mixed boundary conditions that guarantee such symmetry: depending on the fracture mode, some stress components are dropped inside the crack on the crack plane, while certain velocity components are equal to zero outside the crack on the crack plane. Because we should take into consideration complex crack geometries, we should not take advantage of such a symmetry even for the case of planar cracks. Therefore, we only impose stress boundary conditions inside the crack, and

deduce wavefields anywhere else by solving the partial differential eq. (1). We have verified that velocities outside a horizontal crack, on the crack plane, are automatically equal to zero in a homogeneous medium, thanks to the symmetry of the spatial finite-difference stencil. Authors such as Olsen *et al.* (1997) and Madariaga *et al.* (1998) have used fourth-order spatial operators for mixed boundary conditions within a fault zone discretized by two planes of gridpoints. As a consequence, they improved precision of wavefields (especially the high-frequency content) near the crack tip compared with previous results (Madariaga 1976; Virieux & Madariaga 1982). An alternative methodology for mixed boundary conditions has also been proposed by Nielsen & Olsen (1998) reducing spurious oscillations by spatially matching the friction and the slip on the same grid nodes. In the present work, because stress components are defined at the same gridpoints, we proceed in the following way for setting local boundary conditions.

Let us consider a local Cartesian reference frame, $x' - z'$, that matches the crack orientation at a given stress gridpoint of the new staggered grid (Fig. 2). The crack orientation angle with respect to the absolute Cartesian coordinate system, $x - z$, is denoted by θ. Thus, applying a second-order invariant transformation, we may express the stress tensor in the new rotated frame of reference $x' - z'$, in terms of the non-rotated stress components σ_{ij}, as follows:

$$\sigma_{mn} = \sigma_{ij}\beta_{mi}\beta_{nj} \tag{3}$$

where β_{kl} are the director cosines of the rotation matrix associated with the rotation of axes. The components $\sigma_{x'z'}$ and $\sigma_{z'z'}$ in eq. (3), from now on respectively denoted by τ and σ, correspond to the tangential and normal stresses to the crack point (see Fig. 2). For in-plane conditions, one has to specify the shear stress τ, which in general is assumed to drop down to its dynamic friction level as a function of the normal stress σ and the friction coefficient. Once the shear stress is imposed at a given crack point, we transform the stress tensor σ_{mn} back to the original coordinate system, $x - z$, by applying the following inverse transformation:

$$\sigma_{ij} = \sigma_{mn}\beta_{im}\beta_{jn}$$

where β_{lk} are the director cosines of the transposed matrices used in eq. (3). Finally, we perform a new time extrapolation of the velocity field by the finite-difference explicit second-order extrapolation in
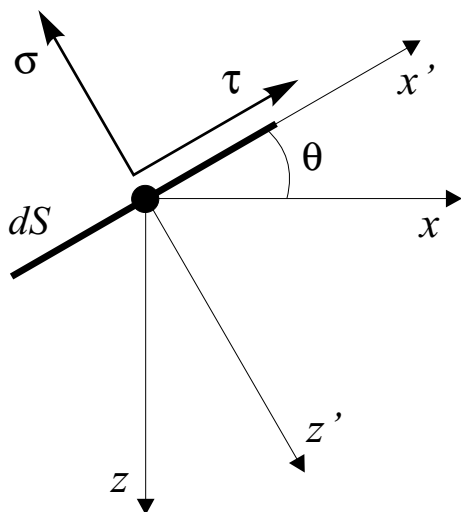
Figure 2. Shear (τ) and normal (σ) stresses acting on a crack surface (dS) tilted at an angle θ with respect to the Cartesian frame of reference $x - z$. The reference frame $x' - z'$ always matches the crack orientation.

time. The above procedure shows the general way we apply the crack boundary conditions in a single stress gridpoint inside the crack. For a numerical analysis of this new strategy for setting local boundary conditions, we shall first consider a crack described by a single point source before handling more complex crack geometries.

4 POINT-SOURCE ANALYSIS

The numerical scaling between the grid spatial size and the physical dimension of a given seismic source allows one to discretize such a source by a different number of stress gridpoints. This is done by adapting the grid size accordingly. As the number of points describing the source increases, we might expect the accuracy of the solution to increase. The velocity grid is still shifted by half the grid step on both Cartesian directions. The slip at a point source can be estimated from the particle displacement values around the point source. Since the slip enters in the rupture failure criterion, an accurate scheme is required. Let us focus our attention on the discretization of a point source before analysing the slip estimation at such a point source.

4.1 Point-source discretization

Let us first consider a point source which emits the same wavefield for any fault orientation. Numerically, several configurations of clusters of stress-grid nodes will satisfy such invariance with respect to the fault orientation. For instance, the simplest configuration is the one-point numerical cell which will not be considered because it provides inaccurate results. The next one is the four-point numerical cell. It consists of four stress-grid points describing one square (black points, Fig. 3a). Similarly, all other cells, nine-point (black points, Fig. 3b), 16-point, 25-point and so on, will also provide the same wavefield for any source orientation. Inside a numerical cell, as an independent unit, the same boundary condition is applied to each stress-grid point. The boundary condition is applied as described in the previous section. Therefore, an oriented seismic point source is represented by one numerical cell, and we expect a better azimuthal behaviour as the number of stress gridpoints increases.

In order to verify the azimuthal invariance of our point-source discretization model, we compare velocity seismograms around one four-point numerical cell for six different fault inclination angles. Results (Fig. 4) show that the point-source model satisfies the wavefield expectation: no significant variations were found for
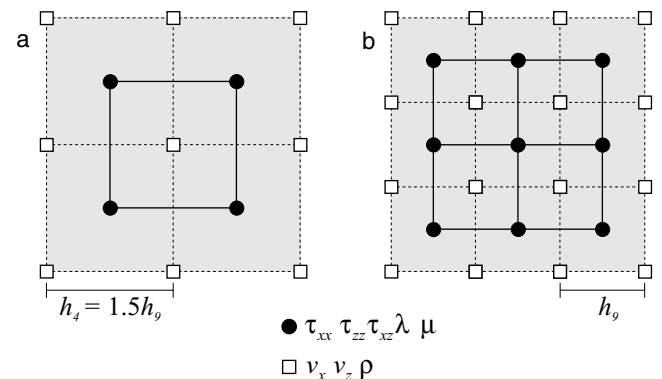
Figure 3. Two equivalent numerical cells: (a) four- and (b) nine-point cells with equal spatial support S (shaded areas). They obey the scaling relation $h_n\sqrt{n} = \sqrt{S}$, where h_n is the grid size associated with a given numerical cell containing n stress gridpoints.
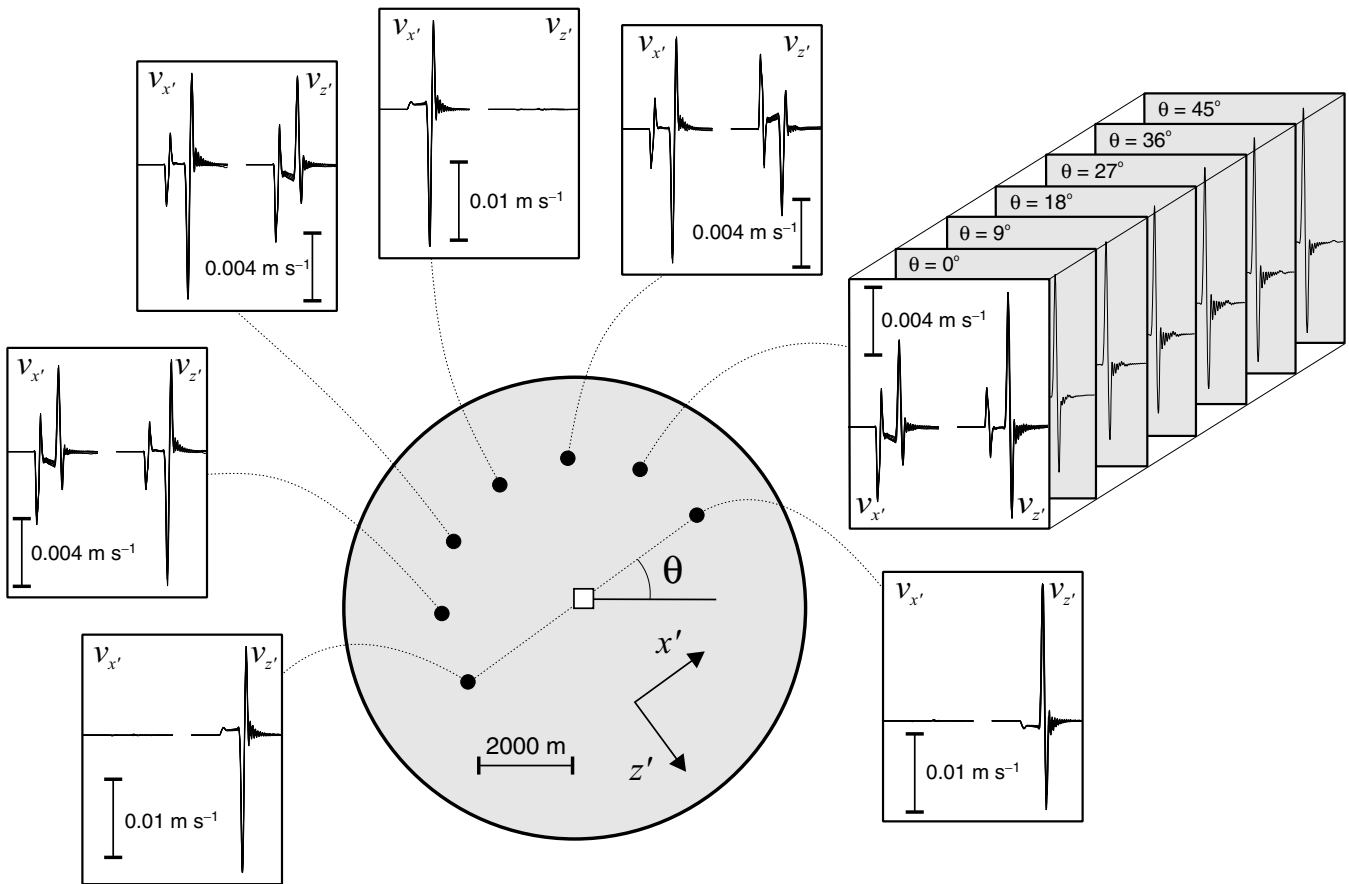
Figure 4. Velocity seismograms (time window 2.4 s) around one point source (white square) for six different fault inclination angles θ computed in seven equidistant positions (black points) with respect to the source. To allow comparison, velocity components were rotated for every θ into the tangential $v_{x'}$ and normal $v_{z'}$ directions to the fault plane, and superimposed (white panels).

different fault orientations. Seismograms were computed in the same seven observational positions (black points) with respect to the point-source (white square) orientation θ. Thanks to the new stencil which regroups the two velocity components in the same grid nodes (Fig. 1b), the velocity field was rotated at each observational point into the parallel ($v_{x'}$) and normal ($v_{z'}$) directions to the fault plane. To keep the high-frequency content of the wavefield under control, we implemented a linear time-weakening constitutive relation. A time lag of 0.1 s was taken for the stress to drop from its initial zero value down to the dynamic level of -30 bar.

Notice the good agreement between the six superimposed traces in each one of the seven observational points of Fig. 4. Even the double-couple radiation patterns of the *P* and *S* wave can be clearly identified. If we analyse the signals in the two observational points that are aligned with the fault plane, we see no ground motion in the parallel component $v_{x'}$. In contrast, we find in the normal component $v_{z'}$ the near-field term deformation with no *P*-wave signature followed by the energetic *S*-wave amplitude. Likewise, similar observations can be made at the middle point that lies perpendicular to the fault plane.

A point source always has a finite support, especially in finite-difference formulations when source discretization is performed as shown in Fig. 3. Discretizing such a source by an increasing number of nodes should lead to similar results if we respect its physical support. This consideration is translated into the following scaling rule for a 2D geometry:

$$h_n \sqrt{n} = \sqrt{S} \tag{4}$$

where the surface *S* is the physical support of the point source (shaded areas, Fig. 3), and h_n is the grid size related to a given numerical cell containing *n* stress gridpoints. So, the same wavefield will be excited by any numerical cell we place inside the surface *S* if the same boundary condition is applied in every node. In other words, whatever the number of stress gridpoints with equal stress drop put inside *S*, the wavefield generated by this seismic source remains identical. To illustrate the scaling relationship (4), we compared seismograms generated with several equivalent numerical cells (Fig. 5). This comparison was carried out for many different fault orientations obtaining basically the same results. However, we found that the content of numerical noise varies with the fault angle, with the maximum level around the middle direction between $0°$ and $45°$. We point out that these two directions are privileged by the spatial differential operators (see eq. 2 and Appendix A). Fig. 5 presents results that correspond to a rather noisy case of a $20°$ tilted source for four-, nine-, 16- and 25-point equivalent numerical cells with a physical support *S* equal to 3600 m^2. Similarly to the simulations of Fig. 4, the same linear time-weakening constitutive law was used to compute seismograms in the same seven observational points (black circles). We observed a good agreement between signals. Both the waveform and the true amplitude of all traces are quite similar to
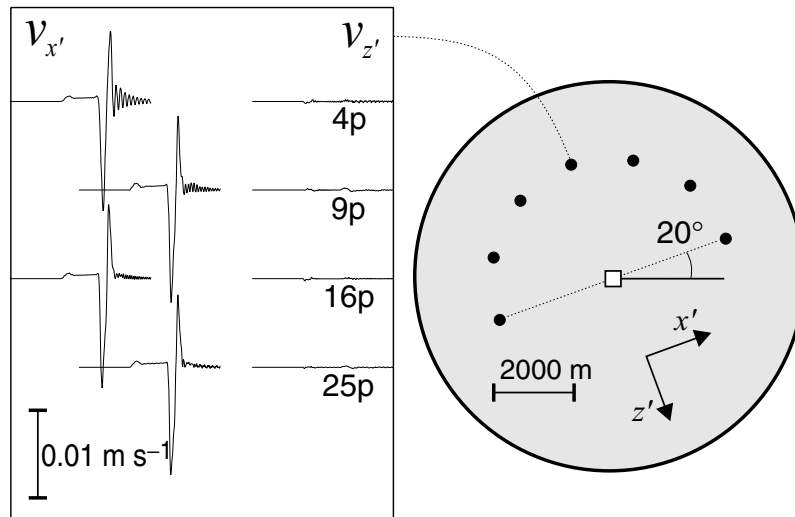
Figure 5. Velocity seismograms (time window 2.4 s) computed around a 20° tilted point source (white square) represented by: four-, nine-, 16- and 25-point equivalent numerical cells.

each other. However, a strong reduction of numerical noise should be noted when considering sources with more than four stress-grid nodes. Exactly the same behaviour was found in the other six observational points not shown in this figure. In accordance with our expectations regarding the numerical scaling, as the order of the numerical cell increases the numerical noise decreases.

4.2 Slip and slip-rate estimation

The second point we address in order to completely describe our point-source model is the slip and slip-rate estimation. The slip function $\mathcal{S}$ on the fault plane is the relative displacement between the positive (D^+) and the negative (D^-) fault blocks as assumed in the following equation:

$$\mathcal{S}(t, \Phi) = D^+(t, \Phi) - D^-(t, \Phi) \tag{5}$$

where the time is denoted by t and the constitutive law by the local set of parameters Φ. We shall assume that the slip will keep the same sign during the rupture process. The fault plane always passes through the centre of the numerical cell (Fig. 6). Thus, velocity gridpoints i around the cell belong either to the positive (p nodes, white squares) or the negative (q nodes, grey squares) fault block. The particle displacement components u_i parallel to the broken surface at these points can be computed by a straightforward integration of the projected velocity field. Hence, for a given set of constitutive parameters Φ, we define the positive fault block displacement D^+ as the average function of the p-weighted particle displacements, $\tilde{u}_i$, associated with the p velocity gridpoints embedded within the block:

$$D^+(t) = \sqrt{\frac{\sum_{i=1}^{p} \tilde{u}_i^2(t)}{p}} \tag{6}$$

where the weighted displacement functions are

$$\tilde{u}_i(t) = u_i(t, \theta)\mathcal{H}_i(\theta) \tag{7}$$

The weight functions $\mathcal{H}_i$ should be defined so that $\tilde{u}_i$ do not depend on θ. In other words, we look for a factor that yields the block displacement D^+ independent of fault orientation. The way the displacements u_i depends on θ can be easily understood as follows. For
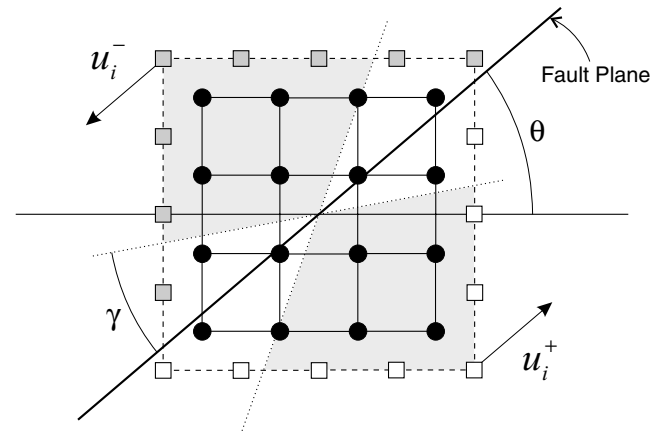
Figure 6. Sixteen-point numerical cell. Both stress (black points) and velocity (squares) gridpoints are separated in two groups by the fault plane (black diagonal line) tilted by an angle θ. The angle γ defines the angular sector (shaded areas) needed to compute the fault slip $\mathcal{S}$ (eq. 5) from individual displacement components u_i (see text).

any time t, the function u_i in a given velocity gridpoint i will be at its maximum if a perpendicular line to the fault plane passing through the centre of the cell coincides with such a point. Conversely, u_i will be at its minimum (i.e. equal to zero) if the fault plane coincides with the point. From this we assume that, for any time t, the maximum value of u_i with respect to θ at a given point i ($\max_\theta\{u_i\}$) corresponds to the reliable displacement value for the slip estimate. Since in general no velocity gridpoint necessarily coincides with the perpendicular line to the fault plane for a given fault orientation θ, the weight functions $\mathcal{H}_i$ must operate over the displacements u_i to yield the maximum values $\max_\theta\{u_i\}$ at every point i. As a result, we could determine the positive block displacement D^+ through eq. (6) independently of θ.

At fixed fault orientation θ, the ratio between $\max_\theta\{u_i\}$ and u_i remains invariable for any time t in every velocity gridpoint i. Consequently, we define the weight functions as follows:

$$\mathcal{H}_i(\theta) = \frac{\max_\theta\{u_i(t, \theta)\}}{u_i(t, \theta)} \tag{8}$$

and found they are time independent. These functions, input into eq. (7), give the reliable displacement value for slip estimate $\max_\theta \{u_i\}$ at every velocity gridpoint i. Functions $\mathcal{H}_i$ are constructed as a function of θ for a given numerical stencil and for a given kind of numerical cell. Because these functions are normalized with respect to the maximal displacement value, they do not depend on the elastic properties of the medium inside which they were constructed. In fact, they represent the radiation pattern of the displacement component parallel to the fault plane seen from every point i around the cell. That is the reason why they do not depend on time. So, once they are computed, they could be stored for future use for boundaries of any shape and propagating medium.

Because the particle displacement u_i at a given velocity gridpoint i tends to zero as the fault plane approaches it, if the fault plane coincides with this point the quotient in eq. (8) becomes infinite. Consequently, there exists an angular vicinity γ around the fault plane (Fig. 6) in which the quotient cannot be accurately determined because the particle displacement is too small. For that reason, to compute the fault block displacement using eq. (6) we always neglect the velocity gridpoints lying inside this vicinity (white areas, Fig. 6). We have found suitable values for γ around $20°$ for point sources. However, as we shall see in the next section, such an angular vicinity will depend on the order of numerical cells when they interact dynamically with each other. In all cases, we also neglect the four velocity gridpoints located at the corners of the cells. There, the displacements are underestimated since they see both sides of the cell.

To determine the negative fault block displacement D^-, we perform the same procedure described in the equations above but considering the q velocity-grid nodes. Finally, one may deduce the slip over the fault plane using eq. (5). The slip-rate is determined in exactly the same way but without integrating the velocity field in the p and q velocity-grid nodes. Note that normalized functions $\mathcal{H}_i$ are valid also for the velocity field.

Fig. 7 shows the evolution of the slip function on one point source for different fault orientations. For these simulations we choose a 16-point numerical cell like the one in Fig. 6. We considered the
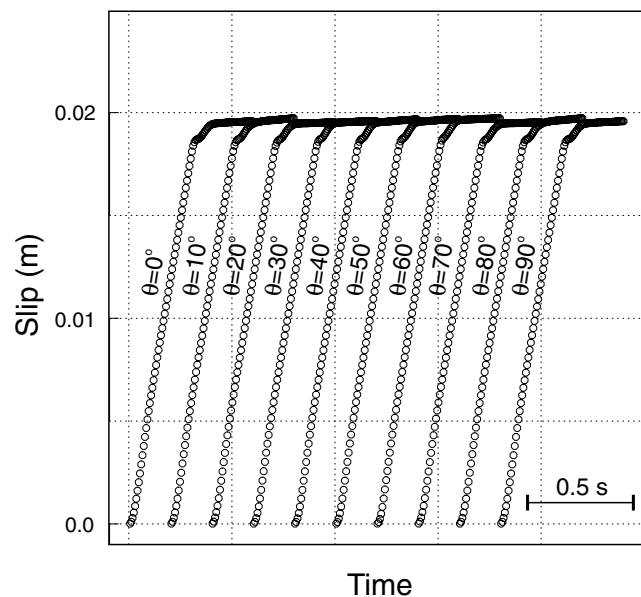
Figure 7. Slip functions (eq. 5) computed for the same point source with 10 different orientations. The source is represented by a 16-point numerical cell (Fig. 6). The slip evaluation is independent of fault orientation.

same time-weakening constitutive relation we used before, condensed into Φ. The only variable parameter between simulations is the point-source orientation. We see that slip functions are not dependent on the source orientation. These results correspond to a particular set of Φ. However, in order to verify that weight functions $\mathcal{H}_i$ are also independent of the constitutive friction parameters, we have performed many tests for different choices of Φ and found the constitutive law to have no influence. Of course, we also verified the general validity of our slip estimation procedure. It works in the same way for any kind of numerical cell we consider.

The accurate estimations of the slip or the slip-rate over the fault plane are key elements for friction behaviour. Rupture simulations with complex friction laws, the slip-weakening one among others, could now be implemented in our numerical model.
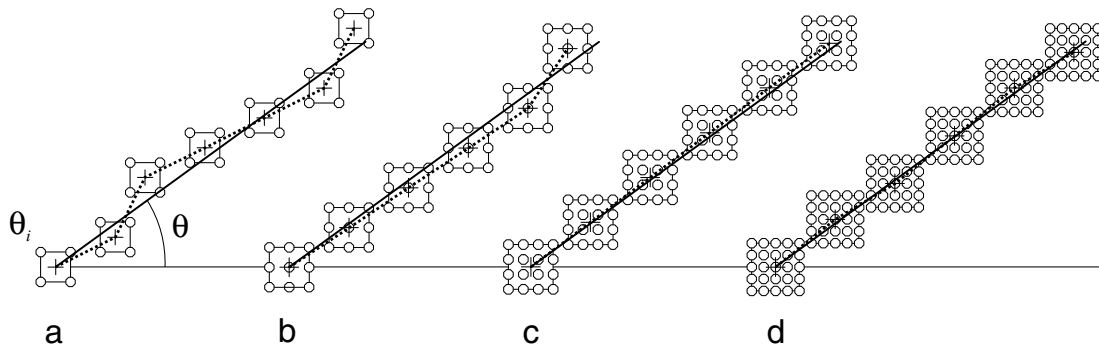
5 PLANAR FINITE SOURCE

A finite source may be thought of as a set of gridpoints which interact dynamically with each other during rupture evolution. This is by no means an addition of single point-source solutions. As a matter of fact, such interaction is the critical issue in our rupture model and we should study how discretization affects numerical solutions. The validation of our finite-source model will allow us to simulate the spontaneous rupture propagation of sources governed by sophisticated constitutive relations in a rather accurate way.
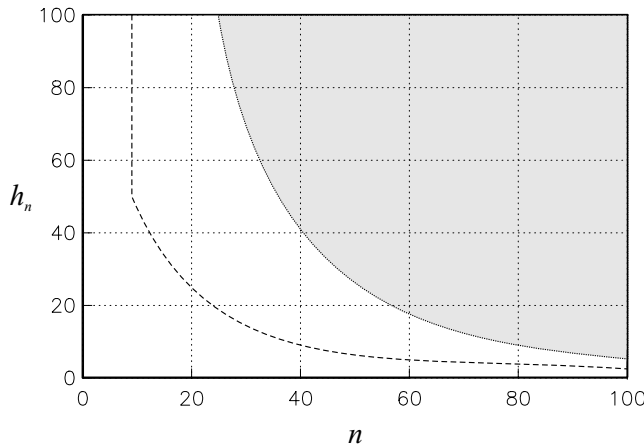
5.1 Numerical accuracy

Numerically, a finite source will be a set of neighbouring cells placed alongside each other without sharing any stress gridpoint (see Fig. 8). In other terms, each stress gridpoint of the source belongs to a single numerical cell. The set of cells should mimic the physical geometry of the fault (solid lines, Fig. 8). Fig. 8 shows how the greater the number of nodes within each cell the smoother the discrete fault geometry (dotted lines) is. Thus, the fault geometry will be fairly well discretized as one increases the order of cells (e.g. Figs 8c and d). The zigzag discrete shape associated with low-order numerical cells (e.g. Figs 8a and b) has unwanted implications for wavefield and fault slip estimation. Depending on the finite-source orientation angle θ, solutions may degrade and hence differ from each other. This is a consequence of destructive dynamic interactions of cells. We apply local boundary conditions in each numerical cell. This means that the individual point-source orientation θ_i in a given cell (see Fig. 8) is the tangent angle to the discrete fault geometry (dotted lines). Consequently, as the number of points within the cells is higher, every θ_i tends to θ thus the destructive interferences tend to disappear, i.e. the degradation of solutions. Generally speaking, the higher the order of cells, the smaller the trace of source discretization in numerical solutions.

A minimal grid size should be considered because of the interaction between boundary nodes. As the grid size is smaller, the dynamic interaction between numerical cells is stronger. For this reason, the smoothness of fault discretization becomes critical when scaling down the mesh spacing. For a given order of cells, there exists a minimal grid size beyond which the interference between cells is destructive enough to perturb solutions. So, in order to solve high-frequency content during rupture modelling by scaling down the finite-difference space increment, we must consider high-order numerical cells to discretize the fault. Fig. 9 illustrates the criterion for numerical accuracy of the boundary conditions we have determined for our finite-source model. This criterion has been determined

Figure 8. Several discretizations of the same planar finite source (diagonal solid lines) for (a) four-, (b) nine-, (c) 16- and (d) 25-point numerical cells. Small circles represent the stress nodes. An individual boundary condition is applied on each cell following the local fault orientation angle θ_i which corresponds to the tangent angle to the discrete source geometry (dotted lines).

Figure 9. Accuracy criterion that relates the grid size, h_n (in m), to the number of stress gridpoints per numerical cell, n, in a given finite source. The shaded area shows the domain inside which numerical solutions are robust for any kind of source geometry. Surprisingly, in order to increase numerical resolution it is not enough to reduce h_n: we also need to adapt the source boundary conditions adding stress gridpoints. Within the region delimited by the dashed line and the shaded area, solutions may disagree up to a factor of 2 as a function of fault inclination. No parabolic correction can be applied there (see text).

experimentally by numerical investigation over a wide range of values for n and h_n. The shaded area represents the numerical domain in which our method yields accurate solutions. It means that, inside this region, solutions are not degraded by destructive interference. Nevertheless, despite the weighting procedure introduced in Section 4.2 we found that, in the case of finite sources, the averaged slip $\mathcal{S}$ (eq. 5) over the rupture surface exhibits a parabolic increase from the reference inclination value at 0° up to a maximum overestimation of 170 per cent at 45°. This angular modulation of the slip amplitude is periodic every 90° and remains the same for any kind of numerical cell we use to discretize the source within the shaded area of Fig. 9. Numerical simulations have shown that neither the rupture evolution nor the exited wavefield are affected by such slip variations when rupture is governed by the slip-weakening friction law. However, we may correct the slip function (eq. 5) for any orientation θ in order to yield its value to the reference one for $\theta = 0°$ by a normalized factor $f(\theta) = A\theta^2 + B\theta + C$, where $A = 0.0002$, $B = -0.0168$ and $C = 1.0$. This factor was also determined numerically, and it yields the slip and slip-rate functions no longer dependent on fault orien-

tation. The dashed line of Fig. 9 represents the numerical boundary over which solutions are perturbed by a factor smaller than 2 with respect to the horizontal reference case. In the region delimited by such a line and the dashed region destructive interactions are important enough to prevent a simple correction such as the one mentioned before which is only valid inside the shaded area.

As we mentioned in the last section, the angular vicinity γ (Fig. 6) required to evaluate the fault slip depends on the order of cells when they interact dynamically. So as to minimize undesired perturbations in the slip function (eq. 5) due to the source discretization, we found that the velocity-grid nodes (squares, Fig. 6) which should be taken into account in eq. (6) are those located as far as possible from the contact zones of the two neighbouring cells. In other words, those points lying in the vicinity of the normal to the local fault plane that crosses the centre of the cell (inside the shaded areas of Fig. 6). Therefore, we have deduced a formula to determine γ that optimizes the slip evaluation in finite sources taking account of the aforementioned consideration. This formula is defined in terms of n, the number of stress gridpoints per cell, and states that $\gamma = \arctan(\sqrt{n} - 1)$. Geometrical considerations lead us to deduce this equation that guarantees, for any kind of numerical cells, at least one, and maximum two velocity nodes inside the shaded area of each fault block.

The scaling relationship that ensures the equivalence between different point sources (eq. 4) is still strictly valid for finite-source modelling. However, finite sources present a length L that is usually much greater than the numerical source thickness T. On that account we should expect some threshold value for the aspect ratio beyond which solutions for different source discretizations are similar (i.e. different thicknesses or kinds of numerical cells). Numerical tests for different combinations of L and T have confirmed this hypothesis, revealing such a geometrical condition. It tells us that the fault aspect ratio must be smaller than approximately 0.033. In other terms:

$$L \gtrsim 30.0 h_n \sqrt{n} \qquad (9)$$

where $h_n \sqrt{n}$ is equal to T and h_n is the grid-space increment related to a given order of numerical cell containing n stress gridpoints. Eq. (9) represents an efficient criterion to guarantee the low-frequency equivalence between different finite-source discretizations. One straightforward consequence of this condition is that we are not obliged to consider a fine mesh in large-scale simulations to maintain the same numerical accuracy. This means that a considerable coarse mesh would be enough to obtain similar low-frequency results. Of course, if we are looking for high-resolution

modelling, then we should reduce the spatial grid size h_n, being always aware of the accuracy criterion shown in Fig. 9.

5.2 Self-similar constant-velocity crack

Kostrov (1964) has constructed a closed-form solution for a self-similar crack propagating at a constant velocity. This analytical example may be used to validate numerical solutions. Yet dynamic crack growth always exhibits numerical instabilities that are caused by the discrete grid-step advance of the fracture edge. Previous works have found inaccurate numerical solutions for the self-similar case, especially when evaluating the shear stress concentration due to the *S* wave travelling ahead of the rupture front (Virieux & Madariaga 1982; Trifu & Radulian 1985). This problem mainly arises from the application of low-order spatial differential operators. More recent finite-difference investigations have reduced this problem by increasing the spatial support of derivatives and by improving the source boundary conditions (Madariaga *et al.* 1998). On the other hand, the spurious oscillations associated with rupture growth can be controlled if dissipation terms are introduced in the formulation of the problem (Knopoff & Ni 2001). These kinds of artefacts indeed help us to clean up numerical solutions. Nevertheless, they will not necessarily improve the accuracy of the stress field determination (Kame & Yamashita 1999) for instance. Thus, to validate our finite-source discretization model introduced in the last section, we have performed self-similar crack simulations without any kind of dissipation terms for different crack inclination angles with respect to the finite-difference grid. Taking account of these artefacts may reduce our requirements, allowing faster simulations.

The Kostrov solution corresponds to a planar source geometry. So, in order to well discretize such geometry for any crack orientation θ, we have used high-order numerical cells (100-point cells). As a result, for every orientation θ, the discrete fault traces are smooth enough to fairly represent the straight crack shape. The rupture is bilaterally symmetric and propagates in a Poissonian medium at 0.5α, the *P*-wave velocity. The value of the shear stress τ drops abruptly from the pre-stress level to some lower level, say τ_f, the dynamic frictional stress. All stresses were normalized by the stress drop $\tau_0 - \tau_f$, where τ_0 is the initial state of stress, so that all results presented here are for a dimensionless stress drop equal to unity.

Figs 10(a) and (b) show, respectively, the slip and the shear stress evaluation at four equidistant points placed along the crack plane for six different inclination angles with respect to the horizontal Cartesian axis. Although oscillations could be observed, the overall estimation is accurate and fits the analytical predictions quite well. We have performed the same test discretizing the source with numerical cells of smaller order, finding less accurate results. As we explained in the last subsection, there is a geometrical factor behind this problem that determines the way the cells interact. Because the analytical solution corresponds to a straight rupture surface, we must consider high-order numerical cells (see Fig. 8) in order to reasonably mimic this specific source geometry and hence to achieve high-resolution simulations without unwanted cell interaction. On the whole, we may conclude that numerical shear stress and slip computation for any fault angle is accurate enough for dynamic rupture modelling with slip or slip-rate dependent friction behaviour. Solutions do not depend on fault orientation. Furthermore, we have checked that as we increase the order of numerical cells not only are the elastic fields better determined, but also the observed spurious oscillations decrease.

5.3 Constitutive friction law

At the present time, many questions about earthquake mechanics have been answered thanks to complex frictional models which have emerged from laboratory experiments (see Scholz 1998, and references therein). The main root of these quite predictable models lies in the tectonic observation that earthquakes happen almost always on pre-existing fault surfaces or at tectonic plate boundaries. This means that both rupture initiation and propagation are frictional rather than fracture phenomena. However, we have not yet studied the aforesaid complex constitutive relations in our numerical modelling. Instead, we have chosen the widely accepted slip-weakening (SW) friction law (Ida 1972; Andrews 1976) for our first investigation of rupture properties. The whole seismic cycle as a consequence of a regular stick-slip frictional instability as well as rupture pulse characterization, for instance, can be explored in future works with our new approach if constitutive relations depending on slip rate, time or state variables are taken into account (e.g. Ruina 1983; Nielsen & Carlson 2000).

The SW friction law we have tested depends on the initial shear stress on the fault surface, τ_0, and the three constitutive parameters cohesion strength, τ_u, dynamic shear stress level, τ_f and characteristic weakening length, δ_0 (Andrews 1976). Mathematically, the way the shear stress τ depends on the slip $\mathcal{S}$ is expressed by the following equation:

$$\tau = \begin{cases} \tau_u - (\tau_u - \tau_f)\mathcal{S}/\delta_0 \; ; & 0 \leq \mathcal{S} \leq \delta_0 \\ \tau_f & ; & \mathcal{S} > \delta_0. \end{cases} \tag{10}$$

We should point out that Coulomb-type friction laws could also be easily integrated, for example, in a similar way as proposed by Aochi *et al.* (2002) because normal (σ) and shear (τ) stresses are computed at the same grid nodes (see Figs 1b and 2). The material strength is finite. Hence, the shear stress concentration near the crack tip is bounded to some prescribed yield value. In the friction model we have chosen (eq. 10), such a value corresponds to the strength τ_u. Once the yield stress is reached at a given fault point, stress drop begins with increasing slip.

According to eq. (10), in order to estimate the shear stress within the cohesive zone we need the slip which, in turn, requires the shear stress to be computed. So, to initiate the rupture in a given fault point, we perform an iterative procedure for shear stress and slip estimations: once the yield stress has been reached, we drop the shear stress to the friction level τ_f, we deduce the slip after one time step by finite-difference integration, we obtain a new shear stress via the friction law (eq. 10) to restart, one time step back, a new slip computation. We stop iterating when a small enough variation in slip is found. In this way we are able to know the next stress state after rupture initiation to continue the stress drop according to our linear constitutive law for successive time step extrapolations. During rupture process, the same shear stress is applied equally at each node of the concerned numerical cell following the procedure described in Section 3.

Fig. 11 displays several phase diagrams for one point in the middle of the source during spontaneous rupture propagation. The relation between pairs of parameters allows one to check the accuracy of the implementation of the constitutive law (Fig. 11a) and wavefield estimate. The elastic properties of the homogeneous medium are shown in Table 1. For this simulation we have chosen the following constitutive values: $\tau_u = 13$ bar, $\tau_f = -33$ bar and $\delta_0 = 0.4$ m, with an initial shear stress $\tau_0 = 0$ bar. To initiate unilateral rupture, we impose rupture in a nucleation zone 2 km long at one extremity of
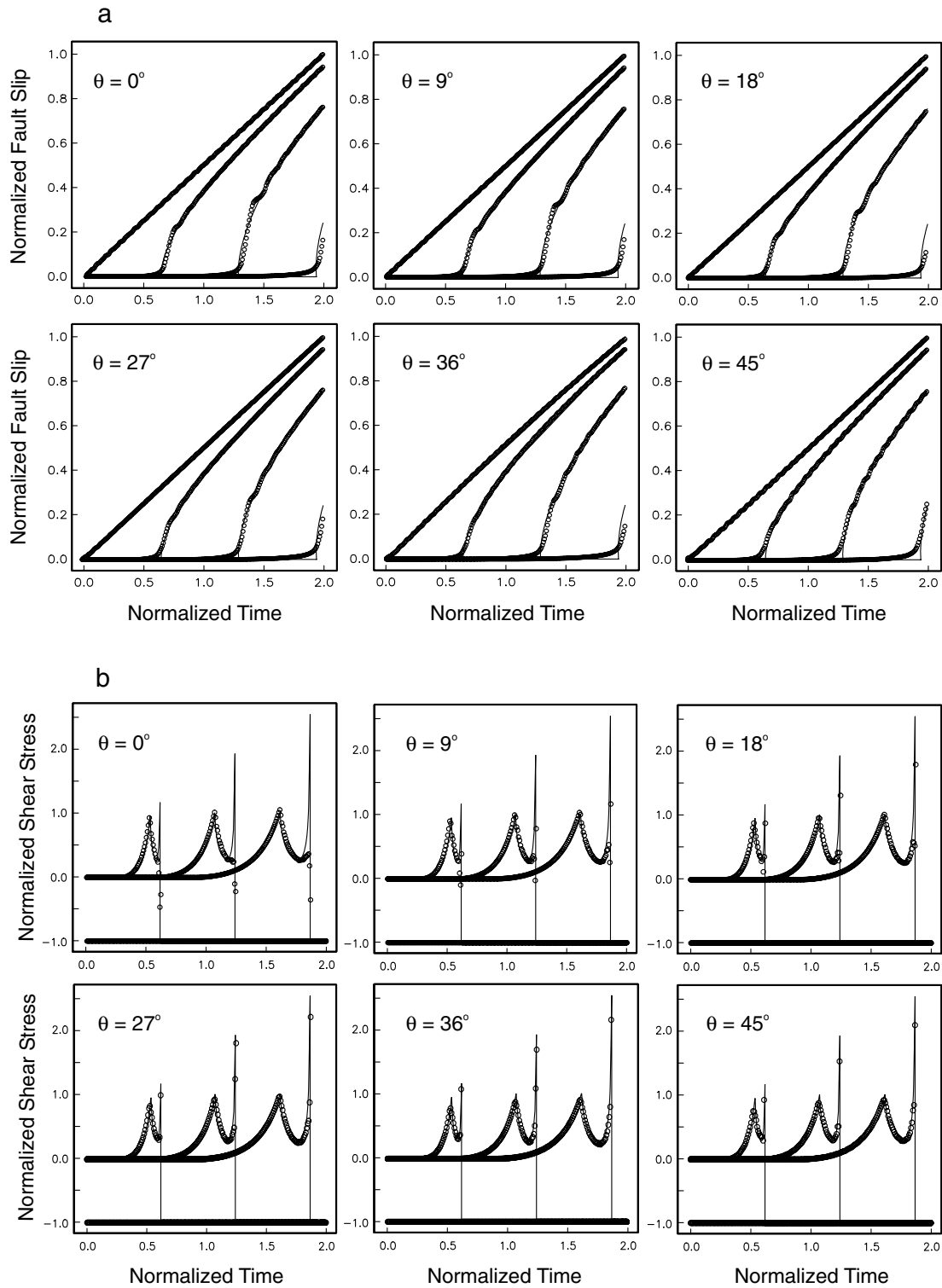
Figure 10. Comparison between analytical (Kostrov 1964, solid lines) and numerical (this work, circles) solutions for (a) fault slip and (b) shear stress at four equidistant points of a self-similar crack propagating at 0.5α, the *P*-wave velocity. Each panel corresponds to a given crack inclination θ with respect to the numerical finite-difference grid. Results should be the same for every θ, only slight oscillations are observed.

a 10 km fault governed by the same parameters except for the yield stress, τ_u, that is assumed equal to the initial stress, τ_0. For this simulation we used 36-point numerical cells with a finite-difference spatial increment $h = 15$ m which is accurate enough for a planar fault parallel to a reference axis. Soon after rupture nucleation, the

rupture front velocity becomes super-shear because of the choice of friction parameters. Das & Aki (1977) have defined the upper yield point parameter S as the ratio between the stress excess $(\tau_u - \tau_0)$ and the stress drop $(\tau_0 - \tau_f)$. Under plane-strain conditions, for values of S less than 1.63, the crack starts growing with a sub-Rayleigh
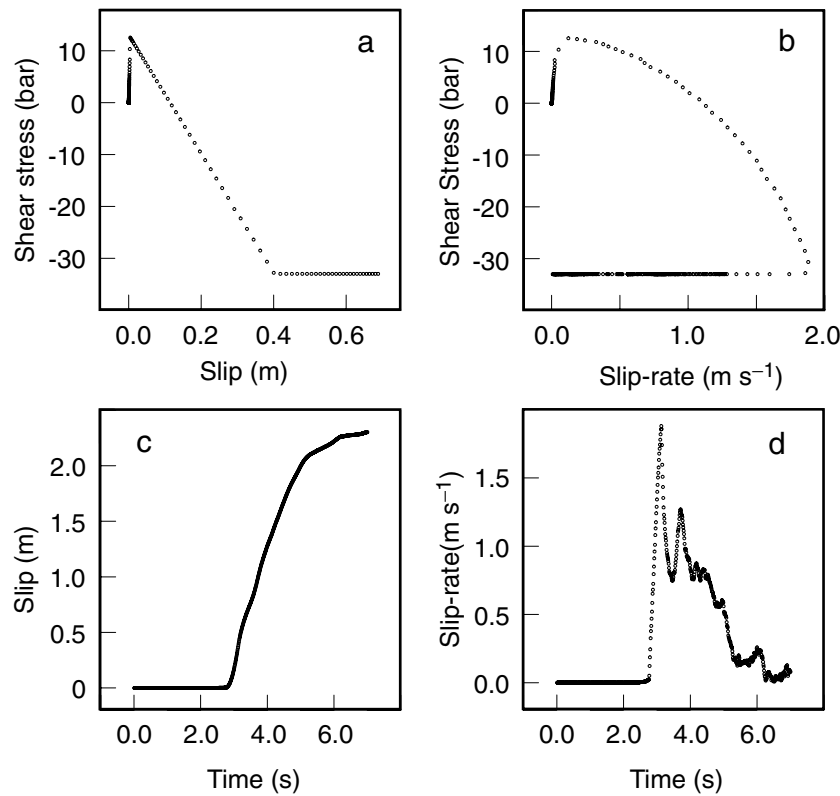
Figure 11. Numerical solutions at a fault point located in the middle of the spontaneous rupture zone governed by the linear slip-weakening friction law (eq. 10) displayed in panel (a). See text for explanation.

Table 1. Velocity structure of the elastic medium used in Fig. 15. V_P and V_S are, respectively, the S- and P-wave velocities, and ρ is the density.

	V_P (m s^{-1})	V_S (m s^{-1})	ρ (kg m^{-3})
Medium	4000	2300	2500
Circular LVZ	2200	1300	1400

velocity, but as its length increases, the velocity changes to supershear and finally approaches the P-wave velocity. That happens in our case given that $\mathsf{S} = 0.39$. As it can be clearly seen in Fig. 11(d), the observational point lies in a fault region for which the rupture front has reached the super-shear regime. Indeed, the slip-rate peak associated with the rupture initiation (around 3 s) arrives before the slip-rate perturbation of the S wave (around 3.5 s) travelling behind the rupture front. After the S wave, we found perturbations due to the back-propagating P- and S-wave arrest pulses around 5 and 6 s after initiation. Only small numerical oscillations are found. Figs 11(a) and (b) show the shear stress evolution as a function of slip and sliprate, respectively. No slip is found before the arrival of the rupture front. By contrast, we see a small increment in the slip-rate just before the material yield stress is reached. This lack of precision can be diminished by scaling down the grid size h. We recall that no boundary condition is imposed in the velocity field outside the crack (see Section 3). Finally, Fig. 11(c) shows the slip history at the same fault point. Slope variations in the slip function around 3.5, 5 and 6 s correspond to the direct S wave and the two aforementioned arrest pulses respectively. Likewise, we may estimate a rise-time of about 3 s.

5.4 Spontaneous rupture propagation

An other way to show how our finite-source model does not depend on fault orientation is to compare solutions for spontaneous sources with different orientations. Similar to the example presented in the above paragraph, the simulations performed for this section also include spontaneous rupture growth governed by the SW constitutive law we have described. In all simulations from now on we took the initial stress state $\tau_0 = 0$ bar and the constitutive parameters over the rupture surface as $\tau_u = 17$ bar, $\tau_f = -20$ bar and $\delta_0 = 0.2$ m. Only the fault orientation angle θ varies. The elastic properties of the homogeneous medium are given in Table 1. We used 100-point numerical cells to discretize the sources in a finite difference mesh of 1200×1200 gridpoints with a spatial increment $h = 10$ m. Fig. 12 shows velocity seismograms for six different fault orientations computed in the same seven positions with respect to the fault plane (black points). So as to allow comparison between different orientations, seismograms were rotated into the parallel ($v_{x'}$) and normal ($v_{z'}$) directions to the fault plane, and then superimposed within the white panels. We considered a final source length of 6 km with a nucleation zone of 1.5 km starting from the left fault edge. We see a good agreement between seismograms for all fault orientations. Because the rupture is governed by the SW constitutive law this implies that the slip estimation during rupture evolution is independent enough of θ to yield the same rupture histories for all cases. Figs 13(a) and (b) show this fact: as a function of time and fault position, our slip and slip-rate estimations on finite sources are satisfactorily independent of fault orientation. As we mentioned before, this feature is important because the dynamic rupture
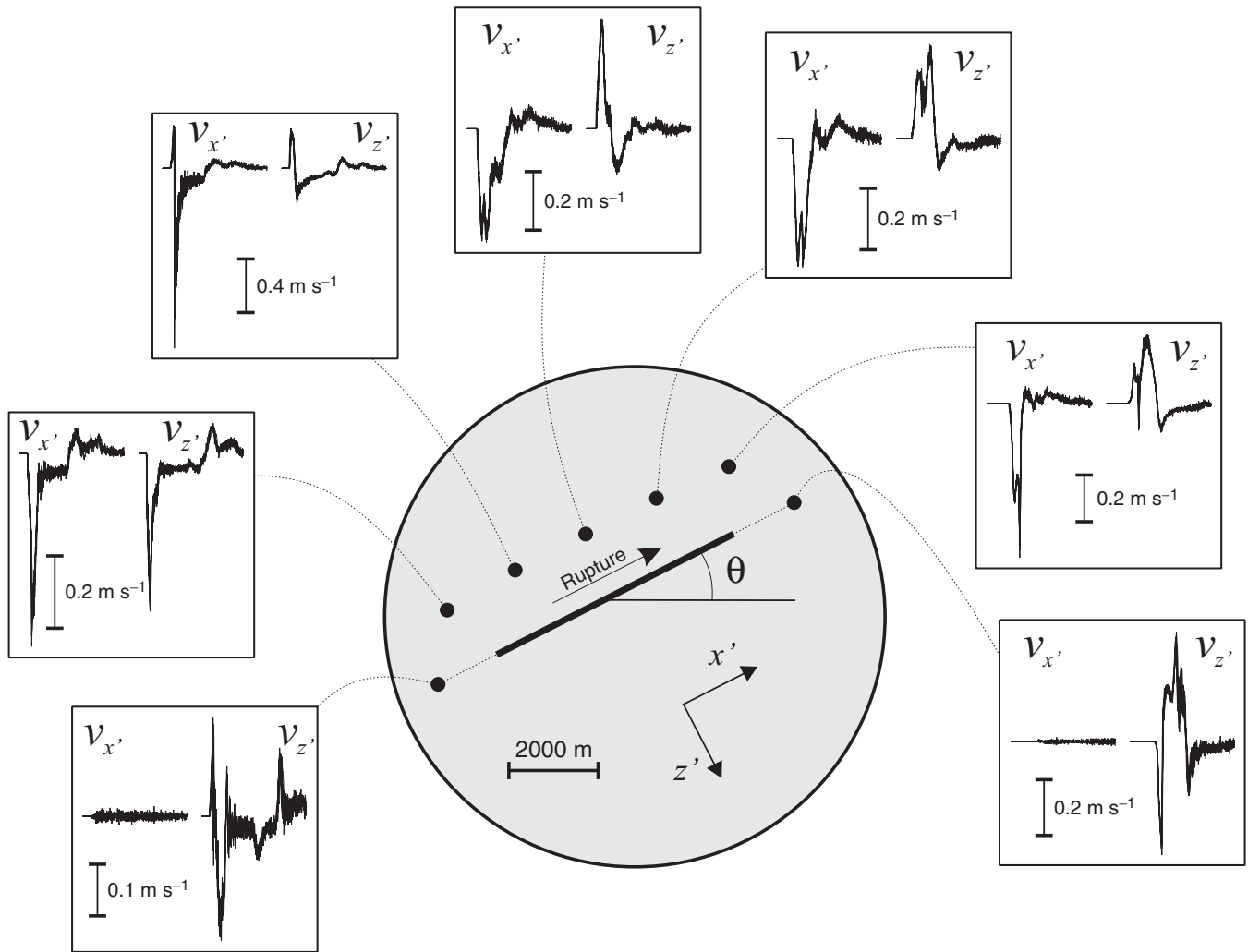
Figure 12. Velocity seismograms (time window 7 s) computed at seven positions (black points) around one finite source (diagonal solid line) for six different fault inclination angles θ ($0°$, $9°$, $18°$, $27°$, $36°$ and $45°$). Velocity components are rotated for every θ into tangential ($v_{x'}$) and normal ($v_{z'}$) directions to the fault plane, and superimposed (white panels). The spontaneous rupture is governed by the slip-weakening constitutive law (eq. 10). The inclination θ only induces numerical noise.

evolution depends directly on the slip $\mathcal{S}$. Any inaccuracy in its estimation may change the rupture history and hence the radiated wavefield.

Looking closer, both figures show the same elapsed time in all cases for the entire rupture. Moreover, as a consequence of the constitutive parameter values, the non-dimensional parameter S is equal to 0.85 (see Section 5.3) and then the rupture front exerts so-called bifurcation (Andrews 1976): soon after rupture nucleation, the rupture front velocity jumps from a subshear to a super-shear regime at the same time for all orientation angles around 0.7 s after rupture nucleation. Figs 14(a) and (b) compare the slip and the slip-rate functions at the mid-point of the spontaneous rupture region for the six fault orientations. We confirm the good estimation of the kinematical parameters independently of θ. We can also identify the S wave travelling behind the rupture front as mentioned before (arrow, Fig. 14b). Furthermore we clearly see the P stopping phase that abruptly changes the slip rate around 2.2 s after rupture initiation (arrow, Fig. 14a) yielding a rise-time of about 2.3 s. Judging from these results, we may say that given the choice of numerical

parameters we are using, oscillations are weak and do not affect the rupture behaviour.

Simulations presented in this section make us confident that spontaneous rupture is adequately modelled when proper source discretization for boundary conditions is performed. This allows us to consider non-planar finite sources as the most sophisticated scenario we are looking for at the current stage of this work.

## 6 NON-PLANAR SOURCES IN HETEROGENEOUS MEDIA

Finite-difference approaches have the capability of propagating elastic waves in arbitrary heterogeneous media by specifying the spatial distribution of elastic properties in the medium. Authors who have studied earthquake dynamics applying these techniques have found how important it could be, in rupture evolution and radiated wavefields, to consider heterogeneous surrounding media (e.g. Harris & Day 1997; Olsen *et al.* 1997; Ben-Zion & Huang 2002). For instance, strong variations in slip and slip-rate over the fault surface, as well

a

b
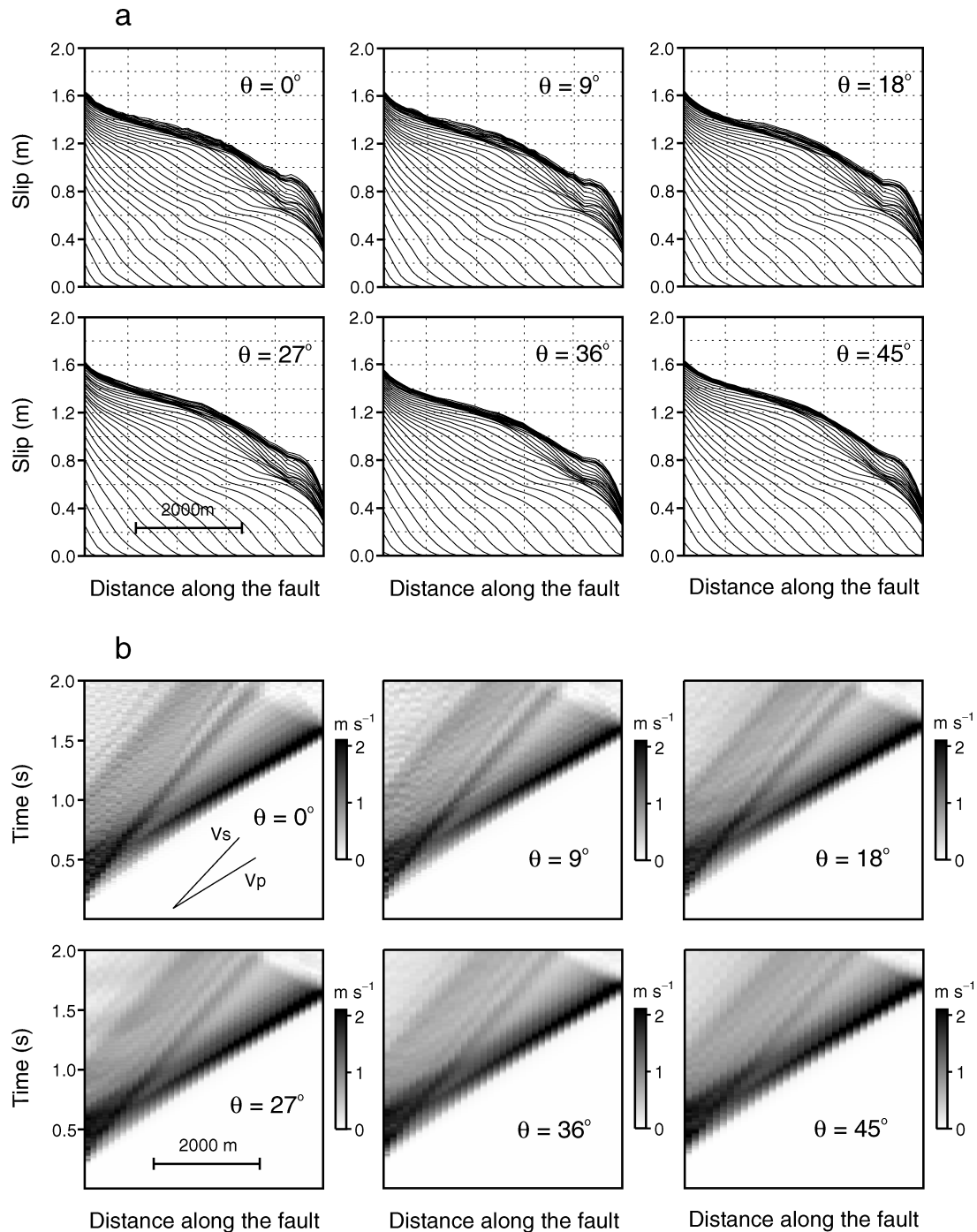
Figure 13. Slip and slip-rate solutions for the finite sources described in Fig. 12. (a) Slip evolution every 0.1 s as a function of fault position. Only reasonably small variations in the slip function are seen depending on fault orientation. (b) Slip-rate as a function of time and fault position. Traces of source discretization are visible as vertical sharp colons associated with numerical cells. However, quite similar results are obtained for all orientation angles θ. Rupture front bifurcation happens soon after spontaneous rupture initiation in all cases.

as in the nature of rupture propagation, have been found. On the other hand, numerical simulations have also shown how important it is to propagate the wavefield through realistic media to explain the observed ground motion in some remarkable cases (e.g. Shapiro *et al.* 2000; Olsen 2000). As we shall see, we are able to introduce this physical consideration during rupture simulations given that our numerical model is based on finite differences.

For modelling finite sources we impose individual boundary conditions at each numerical cell discretizing the fault surfaces. This means that the local fault orientation θ_i (Fig. 8) of every point source depends on its relative position with respect to the immediate neighbouring cells. So far, we have supposed the rupture surfaces to be straight lines in order to simulate planar faults. Nevertheless, the discretization of any kind of geometry in finite-difference modelling
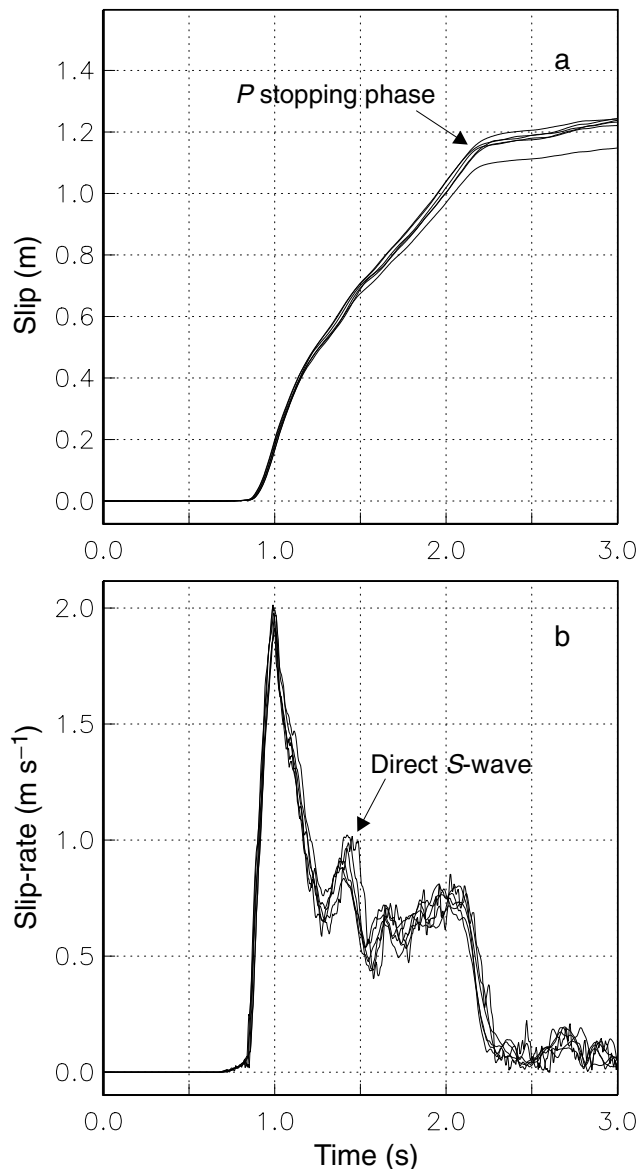
Figure 14. Slip (a) and slip-rate (b) functions computed in the middle-point of the spontaneous rupture region for simulations shown in Fig. 12. The six functions associated with the six different fault orientations are superimposed in both panels.

necessarily has a step or zigzag shape (e.g. dotted lines, Fig. 8) making it difficult to simulate cracks along straight lines, especially when these lines are not parallel to the reference axis. Therefore, from the viewpoint of boundary conditions, discretization of straight or curved lines reduces to the same numerical problem. On that account, the self-similar rupture validation, as well as the spontaneous rupture analysis we have performed for planar sources, ultimately validate our methodology for any kind of source geometry.

So, let us discretize a finite non-planar source following the strategy presented previously, and analyse what happens if we nucleate its spontaneous rupture.

6.1 A realistic example

We carried out the dynamic rupture simulation of an arbitrarily non-planar fault crossing a circular low-velocity zone (LVZ). Rupture

propagation is governed by the SW constitutive relation (10). The goal of this example is not to elucidate the dynamics of such a problem but to illustrate the performance of our new approach under these realistic conditions.

Fig. 15 shows a snapshot of the horizontal particle velocity v_x 4 s after rupture nucleation. The solid black line represents the fault trace which traverses the LVZ (circular dashed line). The elastic properties of both media are shown in Table 1. The fault is 13.8 km long, while the LVZ has a diameter of 4 km. The constitutive parameters along the entire fault are $\tau_u = 15$ bar, $\tau_f = -33$ bar and $\delta_0 = 0.05$ m (see eq. 10). In order to initiate spontaneous rupture propagation we impose rupture along a zone 1 km long located at the left edge of the fault. In such a nucleation region, the initial shear stress $\tau_0 = 0$ is taken as the yield stress, τ_u, to start rupture. We used 100-point numerical cells to discretize the sources in a finite-difference mesh of 1600×1600 grid points with a spatial increment $h = 10$ m.

The unilateral rupture propagates rightwards on a super-shear regime given that S = 0.45 (see Section 5.3). We can clearly appreciate how the shape of the body-wave fronts follow the curved source geometry (Fig. 15). Also as a consequence of such geometry, there exists a focalization of body waves in the upper concave side of the fault, where the particle velocities are considerably greater than those observed on the other fault side (see the imbalance in the grey scale with respect to the zero value). The strongest amplitudes within the LVZ correspond to trapped waves generated during the passage of the rupture front: an energetic back-propagating pulse reflected in the interface between two media, as well as guided waves along the circular elastic boundary, among others. Fig. 16 shows the corresponding kinematical solutions over the rupture surface. The presence of the LVZ has strong implications. First, important velocity changes are exerted by the rupture front depending on the elastic properties of the medium. Second, strong slip (Fig. 16a) and slip-rate (Fig. 16b) concentrations are obtained within the circular low-velocity anomaly. Reflected *P* and *S* waves on the interface between two media are well observed (arrows), especially inside the LVZ where the aforementioned back-propagating *S* wave dominates the later particle motion (see Fig. 16b) provoking a belated sharp slip increment (Fig. 16a). Numerical oscillations can also clearly be seen due to the discrete stepwise advance of the rupture front across the numerical cells (Figs 15 and 16b). However, as we have shown in the last section, these oscillations do not perturb the rupture history.

7 DISCUSSION AND CONCLUSIONS

In this study we introduce a new finite-difference approach to model the dynamic rupture propagation of faults with intricate geometries, e.g. non-planar faults.

A new definition of the crack boundary conditions represents the main root of our approach. Thanks to the spatial stencil we use to discretize the elastodynamic equations, all stress components are known at the same grid nodes. By a simple rotation of the stress tensor, we impose the shear stress drop following the local crack orientation. For accurate slip estimation, we construct weight functions before performing simulations. These functions make the slip estimation independent of source orientation with respect to the numerical grid.

The numerical scaling that exists between the grid size, h_n, and the physical extent of the source, *S*, ensures an infinity of different discrete representations for the same seismic source. The source discretization may be adapted according to the scale of the problem
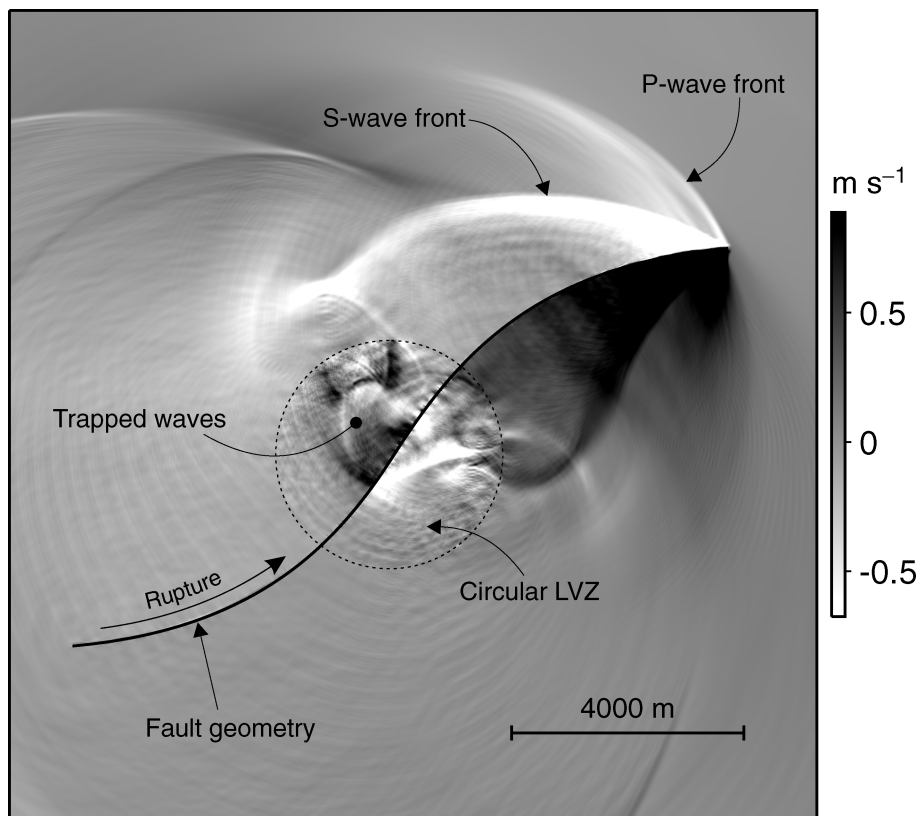
Figure 15. Snapshot of the horizontal particle velocity v_x 4 s after rupture nucleation. The non-planar fault (black curved line) crosses a circular low velocity zone (LVZ, dotted line, see Table 1). Spontaneous rupture governed by the slip-weakening friction law (eq. 10) propagates rightward in a super-shear regime.
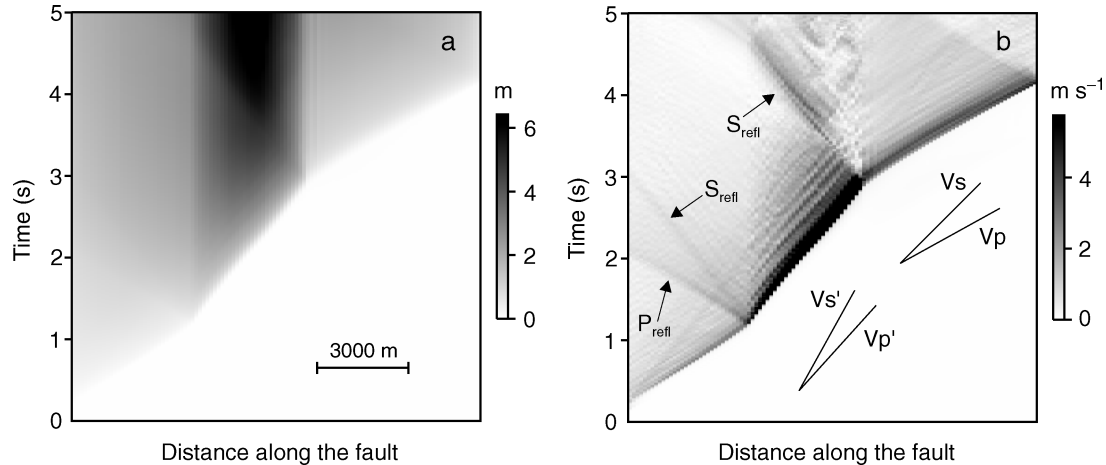
Figure 16. (a) Slip and (b) slip-rate solutions for the simulation shown in Fig. 15 as functions of time and fault position. Straight lines indicate *S*- and *P*-wave velocities within the LVZ ($V_{S'}$ and $V_{P'}$) and within the surrounding media (V_S and V_P) (see Table 1). Arrows point out reflected phases in the interface between two media.

we need to solve. For instance, for the sake of computational efficiency, large-scale numerical simulations may be performed with a few internal source points. Nevertheless, numerical oscillations depend on *n*, the number of stress gridpoints per cell. There exists a strong reduction of noise when *n* is greater than or equal to nine.

High-frequency content in elastic fields near the crack tip is better solved as we decrease the grid size. Similarly, numerical oscillations decrease. However, interaction between internal source points is stronger and source discretization becomes critical. In order to

achieve accurate estimation of kinematic parameters over the rupture surface and exited wavefield, the grid size, h_n, related to a given set of numerical cells with *n* stress gridpoints, must be greater than a lower bound value. We found that the greater the *n*, the smaller the h_n can be. Applying the accuracy criterion we have determined, suitable values for h_n and *n* can be found in order to keep numerical artefacts under control.

Finite sources usually have a fault length *L* much greater than the numerical fault thickness *T*. Thus, the aspect ratio between these two

quantities may play an important role in saving memory resources. The overall features of numerical solution for several sources with length L and different T will be the same if T in all cases is at least 30 times smaller than L. This means that static fault slip, mean waveform and the true amplitude of seismograms are all satisfactorily similar. Because $T = h_n \sqrt{n}$, a minimum number of numerical cells is required to discretize a finite source without perturbing the aforesaid features of solution. In other words, a given finite source must contain at least 30 numerical cells to guarantee the critical aspect ratio. Of course, as we increase the number of cells, i.e. as we reduce the grid size h_n, high-frequency content will be better solved and numerical oscillations tend to disappear.

Because finite-difference approaches are essentially grid methods, from the viewpoint of boundary conditions simulation of non-planar faults is as difficult as simulation of planar faults at an angle with the grid. Only numerical rules for the number of nodes we need to model accurately are essential, and we have determined these rules experimentally. Hence, the comparison with analytical solutions for the self-similar case, as well as spontaneous rupture analysis for planar sources, validate our numerical approach for any kind of source geometry. Results we have obtained for an arbitrary non-planar fault in a heterogeneous medium are in accordance with expectations about the presence of low-velocity zones during the dynamic rupture of faults. Our methodology is robust even in hard conditions.

In order to study the rupture dynamics of real earthquakes, three-dimensional (3-D) numerical models are essential. We think the path leading our rupture model to 3-D space is well highlighted by the methodologies discussed in this paper. On the one hand, the 3-D wave propagation kernel is possible (Saenger *et al.* 2000). On the other hand, the essential element to describe a 3-D source would be the numerical cell translated into a volumetric entity (i.e. a cube). The strategy to evaluate the slip or the slip-rate in 3-D sources should be carefully determined on the basis of the numerical properties of such an elementary cubic cell.

In conclusion, this study introduces a new finite-difference approach to model the dynamic rupture propagation of faults with any pre-established geometry. We have assumed a linear slip-weakening friction law. However, the implementation of Coulomb-type or slip-rate dependent constitutive relations is possible. Thus, our numerical model contributes to the investigation of more realistic scenarios using finite differences by considering arbitrary heterogeneous media, composite friction laws and complex source geometries.

ACKNOWLEDGMENTS

REFERENCES

Andrews, D.J., 1976. Rupture velocity of plane strain shear cracks, *J. geophys. Res.,* **81,** 5679–5687.

Andrews, D.J., 1985. Dynamic plane-strain shear rupture with a slip-weakening friction law calculated by a boundary integral method, *Bull. seism. Soc. Am.,* **75,** 1–21.

Aochi, H. & Fukuyama, E., 2002. Three-dimensional nonplanar simulation of the 1992 Landers earthquake, *J. geophys. Res.,* **107,** doi:10.129/2000JB000061.

Aochi, H., Madariaga, R. & Fukuyama, E., 2002. Effect of normal stress during rupture propagation along nonplanar faults, *J. geophys. Res.,* **107,** doi: 10.1029/2001JB000500.

Ben-Zion, Y. & Huang, Y., 2002. Dynamic rupture on an interface between a compliant fault zone layer and a stiffer surrounding solid, *J. geophys. Res.,* **107,** doi: 10.1029/2001JB000254.

Berenger, J.P., 1994. A perfectly matched layer for the absorption of electromagnetic waves, *J. Comput. Phys.,* **114,** 185–200.

Das, S. & Aki, K., 1977. A numerical study of two-dimensional spontaneous rupture propagation, *Geophys. J. R. astr. Soc.,* **50,** 643–668.

Day, S.M., 1977. Finite element analysis of seismic scattering problems, *PhD dissertation,* University of California, San Diego,

Harris, R.A. & Day, S.M., 1997. Effect of a low-velocity zone on a dynamic rupture, *Bull. seism. Soc. Am.,* **87,** 1267–1280.

Hastings, F.D., Schneider, J.B. & Broschat, S.L., 1996. Application of the perfectly matched layer (PML) absorbing boundary condition to elastic wave propagation, *J. acoust. Soc. Am.,* **100,** 3061–3069.

Ida, Y., 1972. Cohesive force across the tip of a longitudinal-shear crack and Griffith's specific surface energy, *J. geophys. Res.,* **77,** 3796–3805.

Kame, N. & Yamashita, T., 1999. Simulation of the spontaneous growth of dynamic crack without constraints on the crack tip path, *Geophys. J. Int.,* **139,** 345–358.

Knopoff, L. & Ni, X.X., 2001. Numerical instability at the edge of a dynamic fracture, *Geophys. J. Int.,* **147,** F1–F6.

Kostrov, B.V., 1964. Selfsimilar problems of propagation of shear cracks, *J. Appl. Math. Mech. (PMM),* **28,** 1077–1087.

Levander, A.R., 1988. Fourth-order finite-difference P-SV seismograms, *Geophysics,* **53,** 1425–1436.

Madariaga, R., 1976. Dynamics of an expanding circular fault, *Bull. seism. Soc. Am.,* **66,** 639–666.

Madariaga, R., Olsen, K.B. & Archuleta, R.J., 1998. Modeling dynamic rupture in a 3D earthquake fault model, *Bull. seism. Soc. Am.,* **88,** 1182–1197.

Mikumo, T., Hirahara, K. & Miyatake, T., 1987. Dynamical fault rupture processes in heterogeneous media, *Tectonophysics,* **144,** 19–36.

Nielsen, S.B. & Carlson, J.M., 2000. Rupture pulse characterization: self-healing, self-similar, expanding solutions in a continuum model of fault dynamics, *Bull. seism. Soc. Am.,* **90,** 1480–1497.

Nielsen, S. & Olsen, K.B., 1998. A mixed boundary condition for rupture dynamics in finite difference simulations, *EOS, Trans. Am. geophys. Un.,* **79,** F630.

Oglesby, D.D., Archuleta, R.J. & Nielsen, S.B., 2000. The three-dimensional dynamics of dipping faults, *Bull. seism. Soc. Am.,* **90,** 616–628.

Oglesby, D.D., Day, S.M. & O'Connell, D. R.H., 2003. Dynamic and static interaction of two thrust faults: A case study with general implications, *J. geophys. Res.,* **108,** ESE, doi:10.1029/2002JB002228.

Olsen, K.B., 2000. Site amplification in the Los Angeles basin from three-dimensional modeling of ground motion, *Bull. seism. Soc. Am.,* **90,** S77–S94.

Olsen, K.B., Madariaga, R. & Archuleta, R.J., 1997. Three-dimensional dynamic simulation of the 1992 Landers earthquake, *Science,* **278,** 834–838.

Peyrat, S., Olsen, K. & Madariaga, R., 2001. Dynamic modeling of the 1992 Landers earthquake, *J. geophys. Res.,* **106,** 26 467–26 482.

Ruina, A., 1983. Slip instability and state variable friction laws, *J. geophys. Res.,* **88,** 10 359–10 370.

Saenger, E.H., Gold, N. & Shapiro, S.A., 2000. Modeling the propagation of elastic waves using a modified finite-difference grid, *Wave Motion,* **31,** 77–92.

Scholz, C.H., 1998. Earthquakes and friction laws, *Nature,* **391,** 37–42.

Shapiro, N.M., Olsen, K.B. & Singh, S.K., 2000. Wave-guide effect in subduction zones: evidence from three-dimensional modeling, *Geophys. Res. Lett.,* **27,** 433–436.

Trifu, C.-I. & Radulian, M., 1985. Predicted near-field ground motion for dynamic stress-drop models, *Pageoph,* **123,** 173–198.

Virieux, J., 1986. P-SV wave propagation in heterogeneous media, velocity-stress finite difference method, *Geophysics,* **51,** 889–901.

Virieux, J. & Madariaga, R., 1982. Dynamic faulting studied by a finite difference method, *Bull. seism. Soc. Am.,* **72,** 345–369.

APPENDIX A

Saenger *et al.* (2000) have expressed the partial differential operators D_x and D_z in terms of two other operators applied along the main axis of a 45° rotated frame of reference. According to this new definition, we have used the following fourth-order spatial differential operators all through this study:

$$
\begin{aligned}
D_x(f_{ij}) = \frac{1}{2h} \big[& a_0 \left(f_{i+1/2,j+1/2} - f_{i-1/2,j-1/2} \right. \\
& \left. + f_{i+1/2,j-1/2} - f_{i-1/2,j+1/2} \right) \\
& - a_1 \left(f_{i+3/2,j+3/2} - f_{i-3/2,j-3/2} \right. \\
& \left. + f_{i+3/2,j-3/2} - f_{i-3/2,j+3/2} \right) \big]
\end{aligned}
$$

$$
\begin{aligned}
D_z(f_{ij}) = \frac{1}{2h} \big[& a_0 \left(f_{i+1/2,j+1/2} - f_{i-1/2,j-1/2} \right. \\
& \left. - f_{i+1/2,j-1/2} + f_{i-1/2,j+1/2} \right) \\
& - a_1 \left(f_{i+3/2,j+3/2} - f_{i-3/2,j-3/2} \right. \\
& \left. - f_{i+3/2,j-3/2} + f_{i-3/2,j+3/2} \right) \big]
\end{aligned}
$$

where $a_0 = 9/8$, $a_1 = 1/24$ and h is the finite-difference spatial increment.